JOURNAL OF MAGNETIC RESONANCE IMAGING 14:270–280 (2001)

Original Research

Effect of Windowing and Zero-Filled Reconstruction of MRI Data on Spatial Resolution and Acquisition Strategy

Matt A. Bernstein, PhD,* Sean B. Fain, PhD, and Stephen J. Riederer, PhD

Standard, MR spin-warp sampling strategies acquire data on a rectangular k-space grid. That method samples data from the "corners" of k-space, i.e., data that lie in a region of k-space outside of an ellipse just inscribed in the rectangular boundary. Illustrative calculations demonstrate that the data in the corners of k-space contribute to the useful resolution only if an interpolation method such as a zero-filled reconstruction is used. The consequences of this finding on data acquisition and data windowing strategies are discussed. A further implication of this result is that the spatial resolution of images reconstructed with zero-filling (but without radial windowing) is expected to display angular dependence, even when the phase- and frequency-encoded resolutions are identical. This hypothesis is experimentally verified with a slit geometry phantom. It is also observed that images reconstructed without zero-filling do not display the angular dependence of spatial resolution predicted solely by the maximal k-space extent of the raw data. The implications of these results for 3D contrast-enhanced angiographic acquisitions with elliptical centric view ordering are explored with simulations. J. Magn. Reson. Imaging 2001;14:270–280. © 2001 Wiley-Liss, Inc.

Index terms: zero-filling; windowing; spatial resolution; angular dependence; filtering

STANDARD, TWO-DIMENSIONAL spin-warp data sampling strategies acquire lines of MR raw data, each at a particular value of a stepped phase-encoding gradient. These lines of data fill a rectangular k-space grid, which then yields an MR image after reconstruction with a two-dimensional discrete Fourier transform. Here it is explored whether the data in the "corners" of the k-space grid contribute to the useful spatial resolution of MR images. The corners are defined here as the regions outside an ellipse inscribed in the rectangular k-space.

The data in the corners of k-space occupy a large fraction of the total sampled k-space. For example, the area of the inscribed ellipse is $\pi\ k_{x,max},\ k_{y,max}$, where $k_{x,max}$ and $k_{y,max}$ are the extents along the semimajor and semiminor axes, respectively. Since the area of the rectangle is $4\ k_{x,max},\ k_{y,max}$, the corners of k-space comprise $1 - (\pi/4)$, or approximately 21.5%, of the total area. A similar calculation for the three-dimensional case shows that the corners comprise $1 - (\pi/6)$, or approximately 47.6%, of the volume of k-space. These relatively large percentages suggest that an analysis of the value of the data in the corners of k-space has practical implications for the selection of acquisition, windowing, and reconstruction strategies. For example, alternative acquisition strategies such as spiral (1–3), spiral-ring (3), circular echo-planar imaging (EPI) (3), hexagonal (4), and variable encoding time (VET) sampling (5) might be more efficient than Cartesian sampling, in part because they need not acquire the data in the corners of k-space. Moreover, there might be independent reasons for not acquiring the corner data, such as the reduction of acoustic noise (6).

Even if the data in the corners of k-space are acquired, a windowing function (7,8) is often used to apodize it. Windowing can increase the signal-to-noise ratio (SNR), and reduce truncation artifacts, often at the cost of reducing spatial resolution (9,10). The functional form of the windowing kernel, and its parameters and structure are all engineering choices. Determining whether the corners of k-space contribute to the useful spatial resolution is helpful for guiding these selections.

It will be shown that image interpolation plays a role in determining the value of the data in the corners of k-space. Zero-filling (11,12) is an effective and widely used reconstruction method for image interpolation, so it is the sole method considered here. Alternative methods include filling the raw data with noise, rather than zeroes (13). Although zero-filling does not add any information content to the raw data, it can effectively increase spatial resolution by providing overlapping voxels, thereby reducing partial volume artifacts.

THEORY

The effect on spatial resolution of data in the edges and corners of k-space can be illustrated with the calculations presented below. In order to produce simple, analytical results, these examples were based on idealized

Mayo Clinic and Foundation, Rochester, Minnesota.

Presented in part at the 7th Annual Meeting of ISMRM, Philadelphia, 1999.

*Address reprint requests to: M.A.B., Mayo Clinic and Foundation, Charlton 2-223, Rochester, MN 55905.
E-mail: mbernstein@mayo.edu

Received December 6, 2000; Accepted April 9, 2001.

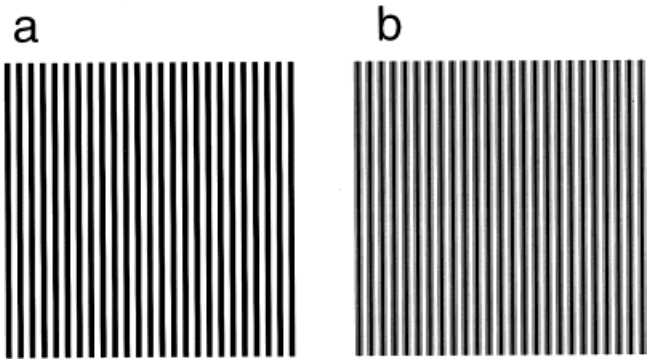

Figure 1. a: A portion of the image represented by Eq. [2], displaying maximal horizontal resolution. **b:** Analogous portion of the image represented by Eq. [3]. In this case, zero-filling smoothes the image, but does not improve the spatial resolution.

raw data sets that are not readily obtained with practical phantoms. Overly broad inferences of the results to more complicated geometries should not be drawn from these calculations. Instead, the purpose of these calculations is to motivate the experimental investigation and discussion that follows.

Illustrative Calculation: the Edge of k-Space

Consider a two-dimensional k-space of size $Nx \times Ny$, with $Nx = Ny = N$, and in which there are only two nonzero raw-data points. Placing one point at the center of k-space and the other horizontally displaced to the edge of k-space, the raw data can be expressed as

$$D_{i,j} = \frac{1}{2}\left(\delta\left(i, \frac{N}{2}\right)\cdot\delta(0, j) + \delta\left(i, \frac{N}{2}\right)\cdot\delta\left(\frac{N}{2}, j\right)\right), \quad i, j = 0, 1, 2, \ldots, N-1 \quad (1)$$

where δ is the Kronecker delta (14) (i.e., $\delta(m,n) = 1$ if $m = n$, 0 otherwise), $i = N/2, j = N/2$ is the center of k-space, and half-pixel effects are neglected since $N \gg 1$. This placement of the two raw data points represents the maximal horizontal resolution available without aliasing with this $N \times N$ k-space, since the two points are separated by the Nyquist frequency in the readout direction, $F_N = Nx/2$. The resulting magnitude image can be reconstructed with a two-dimensional discrete Fourier transform, yielding

$$I_{n,m} = \left|\cos\left(\frac{\pi m}{2}\right)\right|, \quad n, m = 0, 1, 2, \ldots N-1. \quad (2)$$

The magnitude image represented by Eq. [2] only takes on the values 0 and 1, and displays the expected pattern of vertical bars. Figure 1a shows a portion of the image, with $N = 256$. If the raw data in Eq. [1] are zero-filled, and reconstructed on a $2N \times 2N$ array, the resulting magnitude image is

$$I_{n,m} = \left|\cos\left(\frac{\pi m}{4}\right)\right|, \quad n, m = 0, 1, 2, \ldots 2N-1. \quad (3)$$

The magnitude image represented by Eq. [3] now takes on the values 0, 1, and $(1/\sqrt{2})$. Although the resulting image (Fig. 1b) is smoother due to the sinc-interpolation, there is no improvement in resolution compared to the original image, Fig. 1a.

Illustrative Calculation: the Corners of k-Space

Next, consider a second case with only two nonzero raw-data points. Again placing one point at the center of k-space, and this time placing the other in the upper-left corner yields

$$D_{i,j} = \frac{1}{2}\left(\delta(i, 0)\cdot\delta(0, j) + \delta\left(i, \frac{N}{2}\right)\cdot\delta\left(\frac{N}{2}, j\right)\right), \quad i, j = 0, 1, 2, \ldots, N-1. \quad (4)$$

This placement of the two raw data points models the maximal diagonal resolution. The resulting magnitude image can be reconstructed with a two-dimensional discrete Fourier transform, yielding

$$I_{n,m} = \left|\cos\left(\pi\frac{n+m}{2}\right)\right|, \quad n, m = 0, 1, 2, \ldots N-1. \quad (5)$$

The magnitude image represented by Eq. [5] again only takes on the values 0 and 1. However, it displays a checkerboard pattern rather than the expected pattern of diagonal bars. Figure 2a shows a portion of the image, in which we have again set $N = 256$. If the raw data in Eq. [4] are zero-filled, and reconstructed on a $2N \times 2N$ array, then the resulting image is

$$I_{n,m} = \left|\cos\left(\pi\frac{n+m}{4}\right)\right|, \quad n, m = 0, 1, 2, \ldots 2N-1 \quad (6)$$

The magnitude image represented by Eq. [6] now takes on values 0, 1, and $(1/\sqrt{2})$. Unlike the comparison of Figures 1a and b, now zero-filling does improve the spatial resolution; the diagonal bars are clearly resolvable in Figure 2b. This illustrative calculation suggests that data in the corners of k-space do contribute

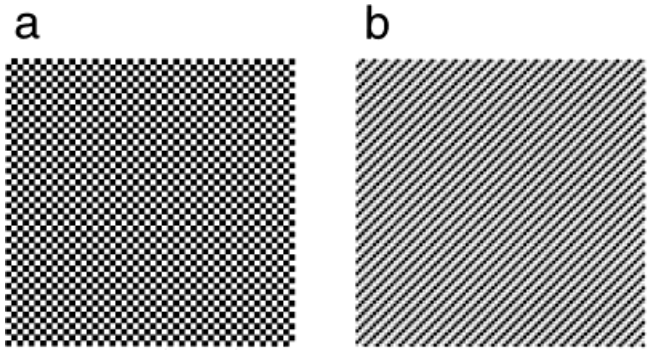

Figure 2. a: A portion of the image reconstructed from data in the corner of k-space, Eq. [5]. Instead of the expected set of diagonal bars, a checkerboard pattern results. **b:** Analogous portion of the image represented by Eq. [6]. Zero-filling improves the diagonal resolution.

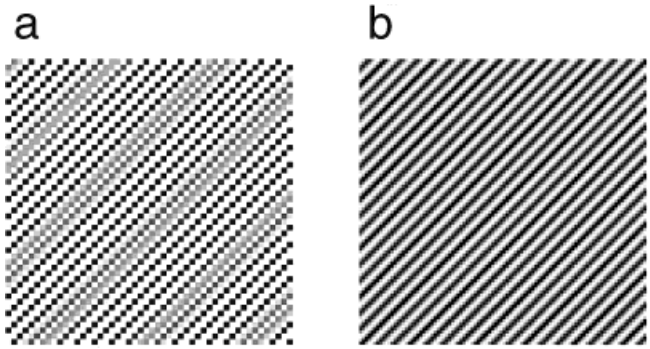

Figure 3. a: A portion of the image represented by Eq. [8]. There is a "beading" artifact and a low-frequency modulation. **b:** Analogous portion of the image reconstructed with zero-filling Eq. [9]. Zero-filling reduces the beading artifact and virtually eliminates the low-frequency modulation.

to the usable resolution of an image, but only when an interpolation method such as zero-filling is used. Interpolation of the *magnitude* image in Figure 2a cannot break the symmetry along the two main diagonals of the checkerboard pattern, and hence cannot provide usable resolution from data in the extreme corner of k-space.

Finally, consider the case of two points separated by a distance in k-space that is numerically equal to the Nyquist frequency along the readout direction, and the separation of which is also diagonally oriented:

$$D_{i,j} = \frac{1}{2}\left(\delta\left(i, \frac{N}{2}\left(1 - \frac{1}{\sqrt{2}}\right)\right)\cdot\delta\left(\frac{N}{2}\left(1 - \frac{1}{\sqrt{2}}\right), j\right) + \delta\left(i, \frac{N}{2}\right)\cdot\delta\left(\frac{N}{2}, j\right)\right), \quad i, j = 0, 1, 2, \ldots, N-1 \quad (7)$$

This case is of interest because the first point is near the margins of data excluded by a radial apodizing window. (Reducing the amplitude of that point by 50% to account for the attenuation of a radial window changes the result quantitatively but not qualitatively, so it does not change the main inferences drawn from this calculation). The resulting magnitude image is

$$I_{n,m} = \left|\cos\left(\pi\frac{n+m}{2\sqrt{2}}\right)\right|, \quad n, m = 0, 1, 2, \ldots N-1. \quad (8)$$

The magnitude image now takes on numerous values, and Figure 3a displays the desired pattern of diagonal bars. As can be seen in Figure 3a, however, the bars display a "beading" pattern reminiscent of the checkerboard pattern in Figure 2a. There is also a low-frequency modulation with a period of approximately seven bars. With the zero-filled reconstruction, the resulting image is

$$I_{n,m} = \left|\cos\left(\pi\frac{n+m}{4\sqrt{2}}\right)\right|, \quad n, m = 0, 1, 2, \ldots 2N-1. \quad (9)$$

As demonstrated in Figure 3b, the beading artifact is reduced and the low-frequency modulation is virtually eliminated, as desired, by the zero-filled reconstruction. Unlike the magnitude image illustrated in Figure 2a, the magnitude image in Figure 3a can be improved by interpolation. This is consistent with previously described techniques that are based on processing magnitude images, and successfully employ zero-filling or sinc-interpolation (15–17).

Radial and Separable Windowing Geometries, and Their Effect on the Corners of k-Space

These illustrative calculations suggest that the effect of zero-filled reconstruction is of particular interest when there are data occupying the corners of the k-space. Whether such data are present depends not only on the acquisition strategy, but also on the windowing applied prior to reconstruction. In digital signal processing (DSP), windows are used to smoothly taper, or apodize, the raw data (7). Apodization reduces or eliminates discontinuities between k-space replicates, thereby reducing truncation artifact (9,10). Apodization can also improve SNR in the image, since the noise power is typically distributed uniformly throughout k-space, while the signal is typically concentrated near the k-space center, which is nearly unattenuated by the window (8,10). (This is in distinction to zero-filling the reconstruction, which can correlate the noise, but does not change the SNR.) Many different windowing functions are used in DSP, and Ref. 7 provides a thorough compilation of one-dimensional window kernels.

Most MRI data acquisitions are two- or three-dimensional, so a two- or three-dimensional window is required. Two possible extensions from one to multiple dimensions are the radial and separable geometries (18–20). Consider, without loss of generality, the two-dimensional case. Given any one-dimensional windowing kernel, $W_{1d}(u)$, where the argument u is normalized so that window full width at half maximum (FWHM) occurs at $u = 1$, the two-dimensional radial window can be written

$$W_{radial}(k_x, k_y) = W_{1d}\left[\sqrt{\left(\frac{k_x}{k_{x,FWHM}}\right)^2 + \left(\frac{k_y}{k_{y,FWHM}}\right)^2}\right]. \quad (10)$$

Normally the k-space FWHM values are simply selected to be half the total extent of the k-space in each respective direction: $k_{x,FWHM} = k_{x,max}$, $k_{y,FWHM} = k_{y,max}$. The two-dimensional separable window can be written

$$W_{separable}(k_x, k_y) = W_{1d}\left(\frac{k_x}{k_{x,FWHM}}\right) \times W_{1d}\left(\frac{k_y}{k_{y,FWHM}}\right). \quad (11)$$

As in Ref. 19, the MR system we used for our experiments employs a radial geometry window, with a Fermi function for the kernel

$$W_{1d}(u) = \frac{1}{1 + e^{(u-1)/T}},$$

$$W_{radial}(k_x, k_y) = \frac{1}{1 + \exp\left(\frac{\sqrt{k_x^2 + k_y^2} - 1}{T}\right)}, \quad (12)$$

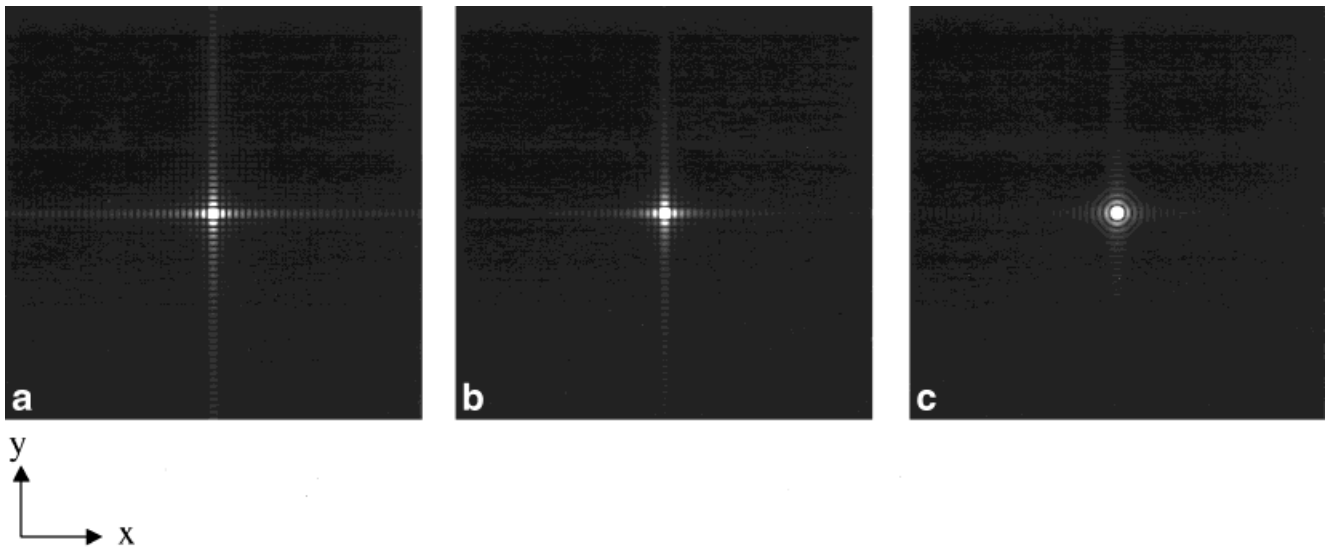

Figure 4. The point spread functions (calculated with zero-filling) for (**a**) no window function, (**b**) separable Fermi window, and (**c**) radial Fermi window. It is apparent when comparing a and b to c that the angular dependence of the spatial resolution is greatly diminished when using a radial window. The residual side-lobes visible along the x and y directions in c result because the radial window has a relatively large value (0.5) at the points ($k_{x,max}$, 0) and (0, $k_{y,max}$). The ratios of peaks of the central to first sidelobe are 4.3, 4.9, and 6.9 for a, b, and c, respectively.

where T is a transition width that is set to $10/(N/2)$, or 0.07813 when $N = 256$. The Fermi window is characterized by a flat passband, and exponential decay in the transition band.

In general, for a given one-dimensional windowing kernel, $W(u)$, the separable geometry admits more of the data from the corners of a two-dimensional k-space than the radial geometry. For example, consider the raw data point displaced from the center k-space along the diagonal, and separated from the center of k-space by the Nyquist frequency along the readout direction. The vector coordinates of this point can be represented as $\left(\frac{k_{x,\max}}{\sqrt{2}}, \frac{k_{y,\max}}{\sqrt{2}}\right)$, the point (0,0) is the center of k-space. Substituting into Eqs. [10] and [12] yields

$$\frac{W_{radial}\left(\frac{k_{x,\max}}{\sqrt{2}}, \frac{k_{y,\max}}{\sqrt{2}}\right)}{W_{separable}\left(\frac{k_{x,\max}}{\sqrt{2}}, \frac{k_{y,\max}}{\sqrt{2}}\right)} = \frac{W_{1d}(1)}{W_{1d}^2\left(\frac{1}{\sqrt{2}}\right)} = \frac{\left(\frac{1}{2}\right)}{0.977^2} \approx 52.4\%, \quad (13)$$

where the numerical values are obtained from the specific form of W_{1d} in Eq. [12]. For the analogous three-dimensional calculation, the resulting ratio is 50.7%. For every commonly used window kernel, the ratio in Eq. [13] is less than unity, indicating that the radial geometry apodizes the corners of k-space more severely.

The SNR increase (8) resulting from the application of a radial Fermi window can be estimated as follows. If the object fills the field of view (FOV), the window apodizes only a negligible amount of low-frequency signal (since $T \ll 1$ in Eq. [12]). It is then reasonable to expect that the SNR increase can be calculated by directly comparing the square root of k-space areas:

$$\frac{\left(\frac{S}{N}\right)_{NoWindow}}{\left(\frac{S}{N}\right)_{RadialWindow}} = \sqrt{\frac{1}{4}\int_{y=-1}^{1}\int_{x=-1}^{1} \frac{dxdy}{1+\exp\left(\frac{\sqrt{x^2+y^2}-1}{T}\right)}} \quad (14)$$

The integral in Eq. [14] can be evaluated with Monte Carlo methods (21) and yields the value 0.87.

For a fixed FWHM of the one-dimensional window kernel, the radial geometry has higher SNR than the separable geometry, since the former apodizes a greater fraction of the noise in the corners of k-space. For a two-dimensional reconstruction and the Fermi window kernel of Eq. [12], calculations similar to those in Eq. [14] show that the FWHM of the separable window must be decreased by 11% compared to the radial geometry to recover this SNR deficit.

Despite its unfavorable SNR properties, the illustrative calculations suggested that the separable geometry can provide superior diagonal resolution when zero-filling is used. This is also consistent with experimental results presented. Figure 4 further demonstrates this effect with grayscale images of point spread functions.

It has been noted that spatial resolution is nonisotropic for Cartesian sampling (20). Based on our theoretical results, we explored this effect further. In particular, we experimentally tested the dependence of the spatial resolution on the angle that a line pair makes with respect to the phase-encoded direction, when the frequency- and phase-encoded pixel sizes are equal. Any increased spatial resolution along the image diagonals is due to the additional, unapodized k-space extent provided by the data in the corners.

METHODS

A resolution phantom with multiple groups of five grooves forming line-pairs with center-to-center spacing of 1.0, 1.20, 1.60, 2.0 mm, etc., was imaged with a 1.5T Signa scanner (General Electric Medical Systems, Milwaukee, WI) with a 256 × 256 matrix, 122 Hz/pixel receive bandwidth, and an FOV of 180 mm. Coronal, 7-mm-thick, full-echo gradient-recalled echo images were acquired each time the phantom was manually positioned from θ = 0–45°, in steps of 5 ± 1°. (To verify that the differences between the phase-encoded and readout directions (such as chemical shift and T2-related blurring) were negligible, an image was also acquired at the 0° orientation with the phase and frequency directions swapped.) Four reconstructions were performed: with and without zero-filling to 512 × 512, and with and without a radial apodizing window (Eq. [12]). The minimum spacing (mm/line pair) resolved in the resulting images was estimated independently by the three authors. Although zero-filling to 1024 × 1024 can provide small incremental gains (11,12), we did not explore that method here since it increases the image size an additional factor of 4, and therefore is not widely used at this time.

Images of the internal auditory canal (IAC) of a normal volunteer were obtained with a 3D fast spin-echo pulse sequence with a 76-mm-diameter loop surface coil. Thirty-two 1-mm-thick sections were acquired in the axial plane. The TR/TE was 2000/104 msec, matrix was 256 × 256, echo train length was 64, and receiver bandwidth was 244 Hz/pixel. The scan time for the single signal average was 4 minutes and 21 seconds. As in the phantom experiment, four reconstructions were performed: with and without zero-filling to 512 × 512, and with and without a radial apodizing window (Eq. [12]). Unlike the phantom experiment, some blurring in the phase-encoded direction was expected due to the long echo train (i.e., 64) of this acquisition.

RESULTS

Figure 5a and b show the measured resolution for each of the four reconstructions (with and without zero-filling, and with and without radial windowing), where the smaller the value (in mm/line pair) the better the resolution. The error bars are the SD of the estimates of the three authors. If the SD was less than 0.025 mm, ±0.025 mm was used for the error bar instead, since it is an estimate of the error due to the discrete spacing of the line pair groups in the phantom. Also plotted on Fig. 5a and b is a dotted curve labeled "cosine reference." This curve is determined by the relation

$$resolution\left(\frac{mm}{linepair}\right) = 2\Delta x \cos\theta, \qquad (15)$$

where Δx = 180 mm/256 = 0.703 mm is the pixel width (and height) prior to zero-filled interpolation. Equation [15] represents an estimate of the expected resolution, in which the factor cosθ accounts for the angular dependence of the maximal k-space extent for a "square" k-space. The factor of 2 in Eq. [15] accounts for the observation that to clearly resolve a line pair, there must be at least one pixel of clear space between the pair, so the center-to-center spacing of the pair is at least two pixels.

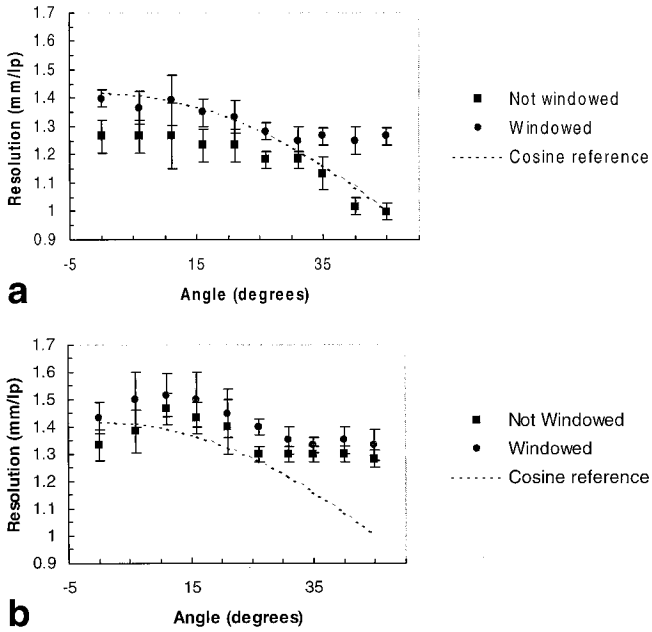

Figure 5. a: Measured resolution as a function of angle, with a zero-filled reconstruction. One set of data was apodized with a radial windowing function. **b:** Measured resolution as a function of angle reconstructed without zero-filling. One set of data was apodized with a radial windowing function.

Figure 5a shows that the measured spatial resolution of unwindowed, zero-filled images significantly improves as the angle θ of the line pairs is increased in the range of 30–45°. The radially windowed zero-filled images, however, show little or no angular dependence of resolution in this angular range, which is consistent with the hypothesis that the data in the corners of k-space cause the angular dependence. The resolution in images reconstructed without zero-filling (Fig. 5b) does not show as strong an angular dependence. We believe that the resolution in these images is limited by partial volume effects.

Figure 6a–d show magnified portions of the images acquired at θ = 45°. Note that without zero-filling, the beading artifact is apparent in the bar patterns and at the edge of the phantom, especially when there is no windowing (Fig. 6b). The smallest group of five bars is only clearly resolved in Figure 6d, which was reconstructed with zero-filling and no windowing. The cost of the improved resolution is apparent from this comparison: Figure 6d has the most severe truncation artifacts. We measure that removing the radial Fermi window decreases the SNR by 17 ± 2% for an object that fills the FOV. This value is in reasonable agreement with the theoretical value of 13% for an object that fills the entire FOV, which was calculated with Eq. [14].

Figure 7a–d shows magnified portions images of the internal auditory canal (IAC) of a normal volunteer. The four reconstruction methods used were the same as in Figure 6: with and without windowing, and with and

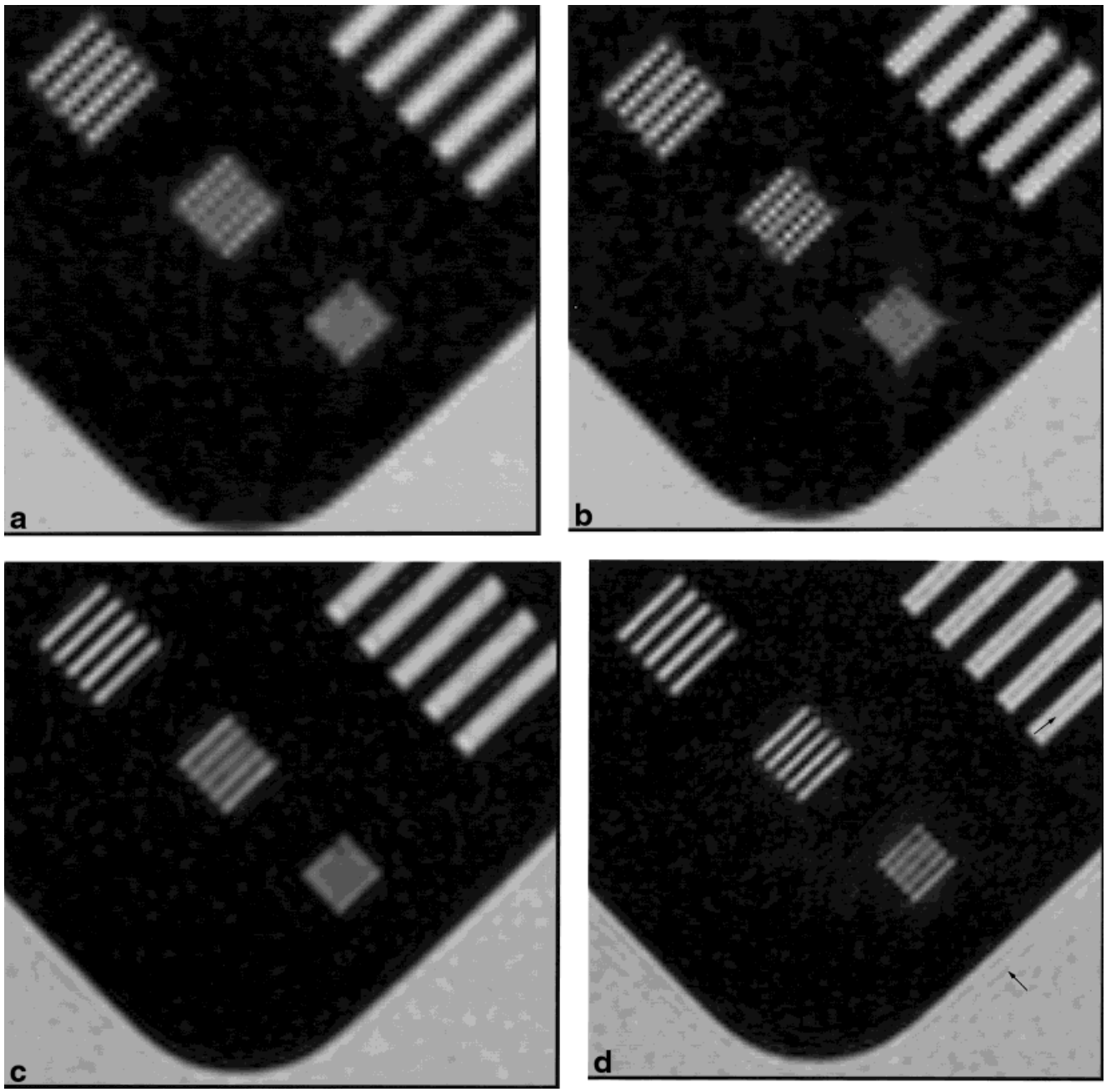

Figure 6. Magnified portions of $\theta = 45°$ phantom images. **a:** Radially windowed, and without zero-filling. **b:** No window, again without zero-filling. Note the beading artifact on both images, and the improved SNR on a. **c:** Radially windowed with zero-filling. **d:** No window, again with zero-filling. Note the smallest group of five bars is resolved only in d. Also note the increase conspicuity of the truncation artifact (arrows) and noise on d.

without zero-filling. Axial, targeted maximum intensity projections are also displayed for each reconstruction method. The IAC was selected because it is a small structure, which is often imaged with high spatial resolution. It has multiple groove and loop structures, and thus can illustrate a clinical application of some of the points raised in this study. A comparison of Figure 7a and d illustrates that zero-filling reduces the beading artifact in the semicircular canals, and increases the sharpness of the scala of tympani and nerves. As in Figure 6c and d, Figure 7c shows increased SNR and reduced sharpness compared to Figure 7d.

Figure 7. Magnified portions of images of the internal auditory canal. The top row shows a single axial section from the 3D set, and the bottom row shows an axial, maximum intensity projection. **a:** Radially windowed without zero-filling. **b:** No window, again without zero-filling. **c:** Radially windowed with zero-filling. **d:** No window, again with zero-filling. Note the reduced beading artifact in the semicircular canals, and the improved sharpness of the scala tympani (i.e., the tympanic canal of the cochlea) in d compared to a.

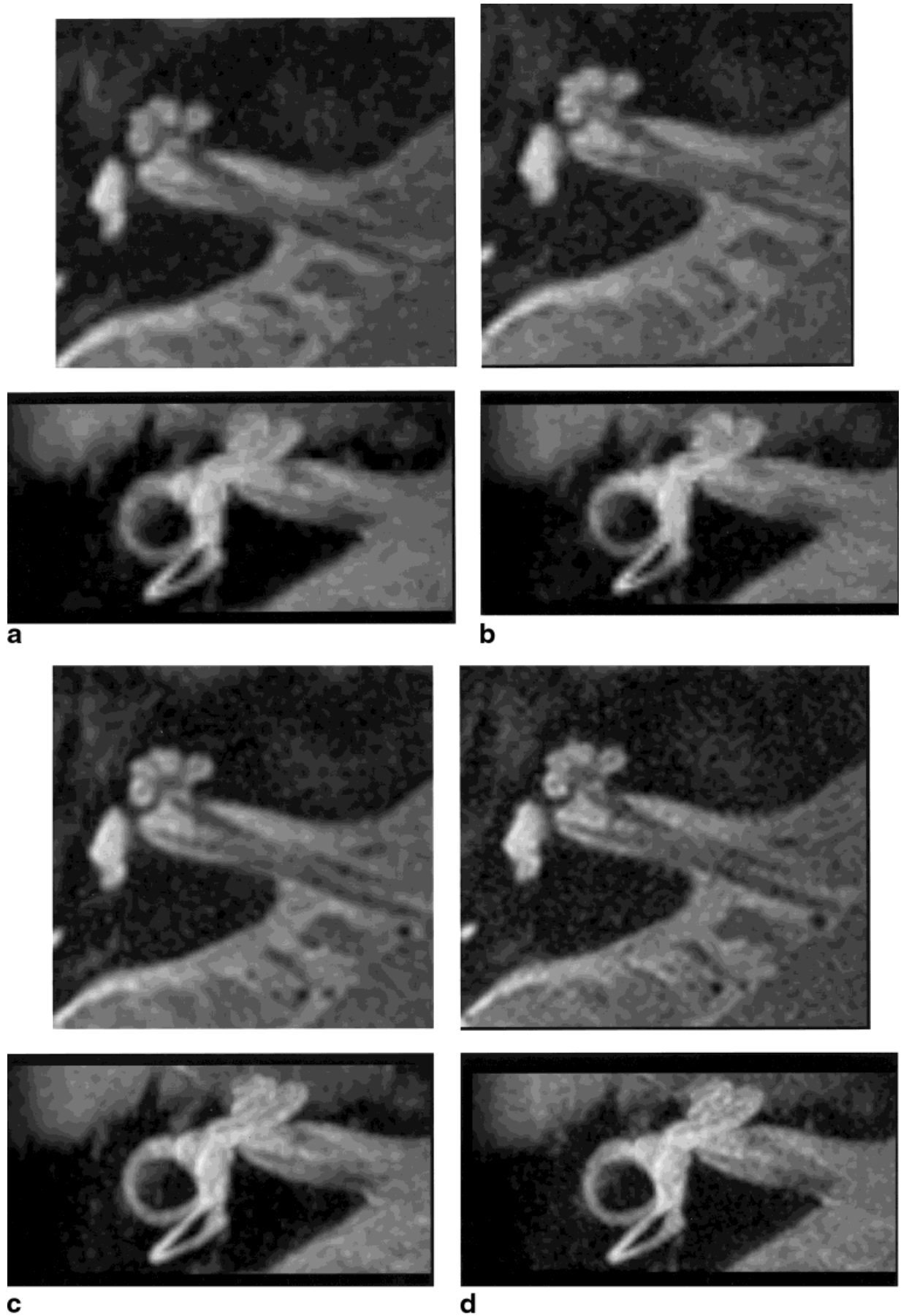

Figure 7.

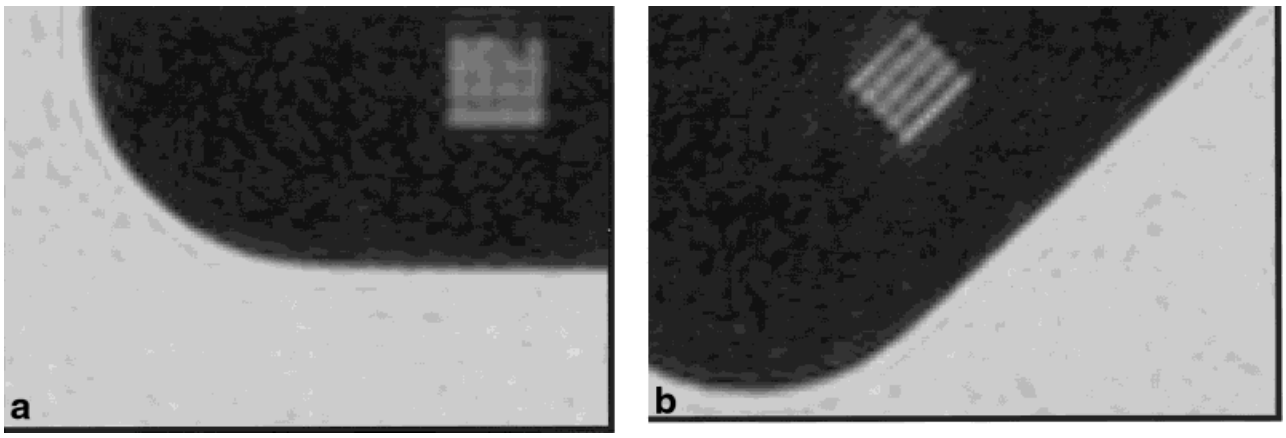

Figure 8. Zero-filled, unwindowed phantom images. Comparison of the smallest group of five bars at (**a**) 0° and (**b**) 45°, displaying the angular dependence of resolution. Note that in addition to blurring, image a apparently depicts only four of the five bars.

Figure 8 shows a comparison of the magnified portion of the phantom images from Figure 6 at $\theta = 0°$ and 45° phantom images with zero-filling, and without windowing. This comparison of images acquired at these two angles demonstrates maximal difference in observed spatial resolution. In agreement with the graph in Figure 5a, the image acquired with $\theta = 45°$ has superior resolution, providing experimental verification that spatial resolution is indeed angle dependent.

DISCUSSION

The benefits of zero-filling described here can be explained by, and are completely consistent with, previous work emphasizing the reduction of partial volume effects (11,12). We believe our discussion of square vs. circular k-space acquisitions is also consistent with previously reported work based on point-spread function analyses (20,22–23). The nonisotropic nature of the angular dependence of resolution with Cartesian sampling was commented upon by Maudsley et al (20) in the context of spectroscopic imaging. To our knowledge, however, we are presenting the first experimental results (except for our own preliminary work (24)) on the angular dependence of spatial resolution, and are the first to demonstrate that the expected diagonal resolution gains are not necessarily realized without special attention to the data reconstruction.

Several inferences with practical implications can be drawn from the results presented here: 1) For data reconstructed without zero-filling, radial window geometry is a reasonable choice since the corners of k-space contribute to the noise but not to the usable resolution. 2) For data reconstructed with zero-filling, separable windowing geometry offers the advantage of admitting more of the corner data, which can improve spatial resolution, while simplifying computation by allowing window application on a row-by-row basis. 3) If a zero-filled reconstruction is not used, scan time is wasted when acquiring data in the corners of k-space. In this case, methods such as spiral acquisitions have an intrinsic efficiency advantage. Conversely, if zero-filling is used, and the corner data are not apodized, acquiring corner data improves the spatial resolution, but the improvement is angle dependent.

We qualify all of these inferences by emphasizing that we have presented a somewhat limited set of object geometries in this work.

As an example of the practical implications of this work, the basic concepts outlined can be applied to a simulation of a contrast-enhanced, three-dimensional MR angiography acquisition. Because of the large fraction of k-space volume they occupy, the corners of k-space play an important role in three-dimensional acquisitions. In addition, it is relatively straightforward to reduce acquisition time by excluding corner data. This can be accomplished simply by not acquiring selected k_y-k_z views. We investigated what happens when we either acquire or exclude corner data, under the constraint that the scan time is held fixed. When the corner data are excluded, the "extra" acquisition time can be used to acquire a larger k-space ellipse, thereby decreasing the voxel size (22,23). This procedure has a proportionate decrease in SNR. To increase its practical relevance, our simulation used elliptical centric view ordering (25,26), and an empirically fitted (27) uptake curve for the gadolinium bolus.

Figure 9a shows a numerically generated bull's-eye pattern that was used to assess spatial resolution, and its angular dependence for the simulation of the contrast enhanced scan. This pattern was Fourier transformed onto a 1024×1024 grid to represent an ideal k-space for the bull's-eye. That k-space was sampled in two separate simulations, using a phase- and slice-encoding matrix size adjusted to maintain a total scan time of 48 seconds, assuming a constant TR of 6.6 msec. A 15.0-cm (phase) $\times$ 6.0-cm (slice) FOV was assumed for both experiments.

For both simulations, the k-space data from the resampled bull's-eye phantom were modulated by the time-dependent intensity of an empirically fit bolus profile. Correct synchronization of the three-dimensional scan was assumed, i.e., the start of acquisition at the center of k-space corresponded to peak contrast enhancement. The empirically fit bolus profile used was measured in the carotid artery of a patient after a 20 cc

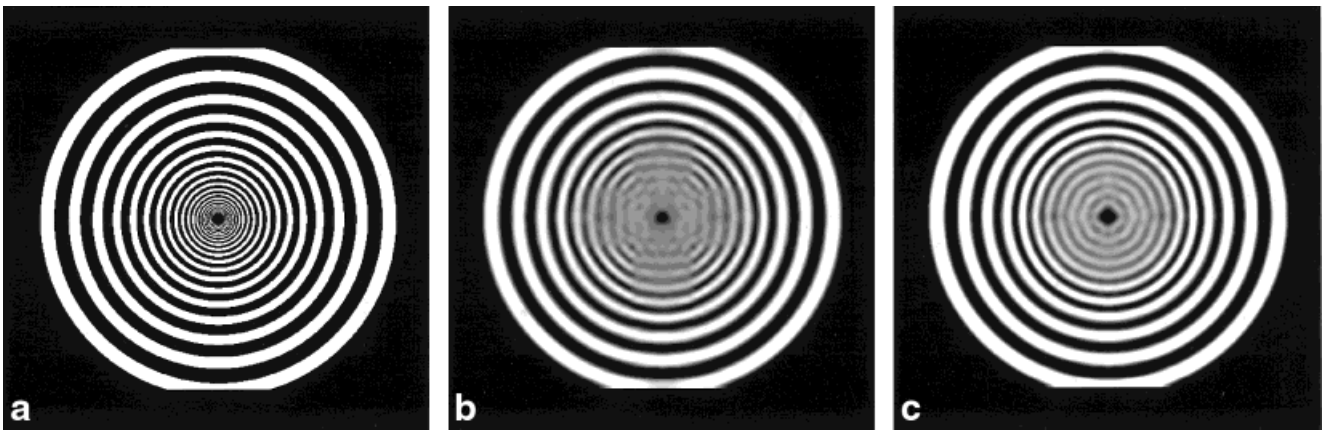

Figure 9. a: Numerically generated bull's-eye pattern. **b:** Simulated image with acquisition of the corners of k_y-k_z space. Note the angular dependence of the spatial resolution. The simulation assumes elliptical centric view ordering, and contrast bolus time dependence. **c:** Simulation image with the acquisition time held constant compared to b, but data in the corners of k-space are not acquired. Instead, that acquisition time is used to increase the spatial resolution. The reconstructions in both b and c are both zero-filled by a factor of 4.

injection of Gadoteridol (Prohance, Bracco Diagnostics, Milan, Italy) injected at 3 cc/second (27).

In the first simulation, the corners of k-space were acquired. Therefore, the matrix size of 134 (phase encoding) $\times$ 54 (slice encoding) was determined by the product of the number of encodings, and the TR. This resulted in a nearly isotropic pixel size of 1.119 mm $\times$ 1.111 mm before zero-filling.

In the second simulation, the corners of k-space were not acquired, but the total scan time was held fixed. Thus the final matrix size of 152 $\times$ 60 is approximately $\sqrt{(4/\pi)}$ larger in the phase- and slice-encoded directions, for a reduced pixel size of 0.9868 mm $\times$ 1.00 mm. We expect that this reduction in voxel size would result in a 9% reduction in SNR in an actual imaging experiment, since the imaging time is held fixed.

Note that when the corners of k-space are acquired, there is an angular dependence of the spatial resolution along the diagonal directions (Fig. 9b). When the corners are not acquired (Fig. 9c), the improved spatial resolution along the diagonal is traded for improved spatial resolution, which is virtually isotropic.

We have shown that omitting the corners of k_y-k_z space while holding the scan time fixed can be a useful acquisition strategy, if a small reduction in SNR is acceptable. It is important to note, however, that the differences illustrated between Figure 9b and c can be greatly reduced in practice when the voxel dimension in the phase and slice directions become more anisotropic. (Calculations that quantify the area in the corners of k-space for the elliptical centric view order are presented in the Appendix.)

CONCLUSIONS

It was shown theoretically and experimentally (at least for some object geometries) that the data in the corners of k-space contribute to spatial resolution along diagonal image orientations when an interpolation method such as zero-filling is used. In the absence of radial data apodization, the expected angular dependence of spatial resolution results, even with Cartesian acquisitions that are isotropic (i.e., equal phase- and frequency-encoded dimensions). When the data were reconstructed with neither windowing nor zero-filling, strong angular dependence of the spatial resolution was *not* observed. This result suggests that spatial resolution is determined not only by the maximal extent in k-space, but also can be limited by effects introduced during the reconstruction process. Thus zero-filling is most helpful improving for resolution along the diagonal direction when the corners of k-space are acquired and retained.

Simulations of three-dimensional data acquisitions with the elliptical centric view ordering and modulation by an empirically-fitted gadolinium uptake curve demonstrate that it can be a useful strategy to not acquire the corners of k_y-k_z space. Instead, the acquisition time saved can be used to improve spatial resolution in an isotropic fashion. It was shown, however, that the relative advantage of this strategy diminishes as the slice- and phase-encoded voxel sizes become more unequal.

APPENDIX

Consider the filling of the k_y-k_z space of a 3D scan acquired with elliptical centric view ordering (25–27). Recall with this view ordering, the distance d from the origin of the k_y-k_z space (0,0) to each view (ky, kz) is calculated. The views are then sorted by d, and acquired in the order of ascending distance. Thus, this view order can be visualized as acquiring k-space views in concentric circular rings which have increasing diameters. As illustrated by Figure 10, an interesting situation with respect to the corners of k-space arises when the aspect ratio A of the k_y-k_z space is not equal to unity. This occurs whenever the voxel dimension Δy is unequal to the slice thickness Δz. Let the aspect ratio be A, and suppose, without loss of generality, the voxel dimension in the phase-encoded direction is the smaller:

$$0 \le \frac{\Delta y}{\Delta z} = \frac{k_{z,\max}}{k_{y,\max}} = A \le 1 \qquad \text{(A.1)}$$

According to Figure 10, k_y-k_z space is filled in a straightforward radial manner until d reaches $k_{z,\max}$. When

$$k_{z,\max} \le d \le k_{y,\max} \qquad \text{(A.2)}$$

the views lying in the shaded region of Figure 10 are not acquired. Once the value $d = k_{y,\max}$ is reached, there are residual corner views that lie outside the larger circle in Figure 10, but still lie within the rectangle. The ratio r of the area of these corner views to the area of the entire rectangular k_y-k_z space can be readily calculated:

$$r(A) = \frac{1}{A}\int_0^A (1 - \sqrt{1 - x^2})dx = 1 - \frac{\sqrt{1 - A^2}}{2} - \frac{\arcsin A}{2A} \qquad \text{(A.3)}$$

The corner-occupation ratio as a function of aspect ratio, *r(A)* is plotted in Figure 11. Note that when $A = 1$ (square k-space) r is $1 - \pi/4 = 21.5\%$, as expected. But as the voxel becomes more anisotropic (i.e., as A approaches 0), the fraction r of the area occupied in the corners drops precipitously. This drop occurs because a circle of radius $k_{y,\max}$ (rather than ellipse) is inscribed in the rectangle. For an inscribed ellipse, which is the appropriate model for windowing k-space where $A \neq 1$, the area in the corners is always $1 - \pi/4$, regardless of the aspect ratio A, as derived in the Introduction.

The time to acquire the views in the corners of the k_y-k_z space can instead be used to increase the spatial resolution, at the cost of SNR. Although the differences in Figure 9b and c are quite apparent, it should be noted that the maximal effect occurs only when the k-space is square ($A = 1$) since that is when the area ratio r is largest. For a typical value of $A = 0.7$, the r is only 0.09, so the difference in the acquisition strategies of Figure 9b and c is reduced by approximately a factor of 2.4.

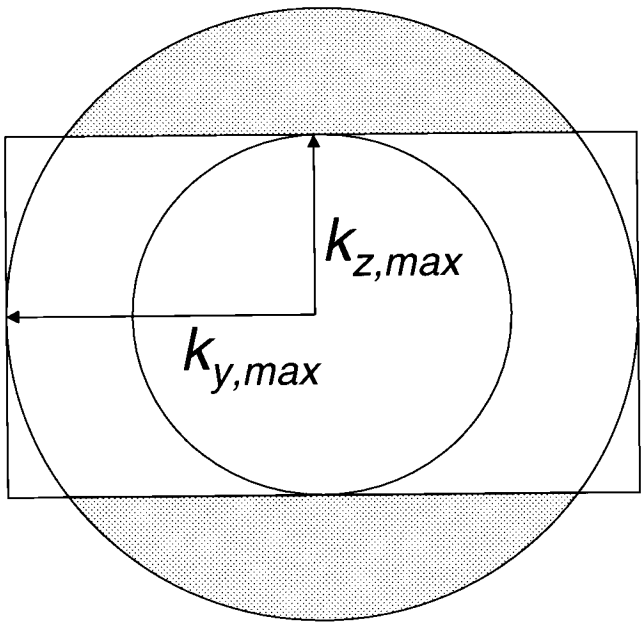

Figure 10. When a three-dimensional k_y-k_z space is filled according to the elliptical centric view order, the data in the corners of k-space occupy a maximal fraction of the entire k-space when the voxel sizes in the slice- and phase-encoded directions are equal.

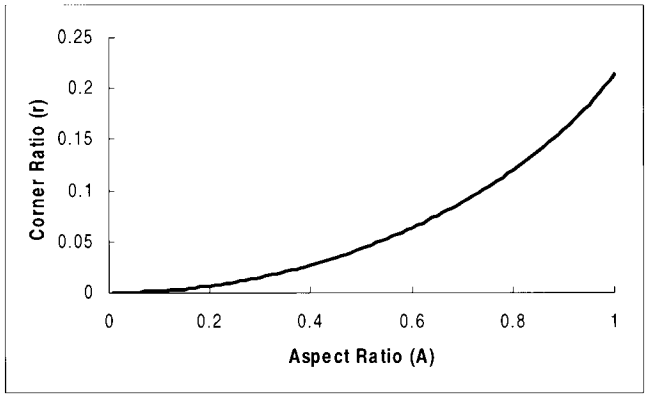

Figure 11. Plot of Eq. [A.3]. This plot suggests that the difference between 3D elliptical centric acquisition strategies that either acquire or do not acquire the corners of k_y-k_z space diminish rapidly as the voxel dimension aspect ratio A decreases.

REFERENCES

1. Ahn CB, Kim JH, Cho ZH. High-speed spiral-scan echo planar imaging. IEEE Trans Med Imaging 1986;MI-5:2–7.
2. Meyer CH, Hu BS, Nishimura DG, Macovski A. Fast spiral coronary artery imaging. Magn Reson Med 1992;28:202–213.
3. Kerr AB, Pauly JM, Hu BS, et al. Magn Reson Med 1997;38:355–367.
4. Ehrhardt JC. MR data acquisition and reconstruction using efficient sampling schemes. IEEE Trans Med Imaging 1990;9:305–309.
5. Feinberg DA. VET imaging: magnetic resonance imaging with variable encoding time. Magn Reson Med 1997;38:7–14.
6. Hennel F. Acoustic optimisation of rapid MRI. In: Proceedings of the 8th Annual Meeting of ISMRM, Denver, 2000. p 2010.
7. Harris FJ. On the use of windows for harmonic analysis with the DFT. Proc IEEE 1978;66:51–83.
8. McVeigh ER, Henkelman RM, Bronskill MJ. Noise and filtration in magnetic resonance imaging. Med Phys 1985;12:586–591.
9. Wood ML, Henkelman RM. Truncation artifacts in magnetic resonance imaging. Magn Reson Med 1985;2:517–526.
10. Parker DL, Gullberg GT, Frederick PR. Gibbs artifact removal in magnetic resonance imaging. Med Phys 1987;14:640–645.
11. Parker DL, Du YP, Davis WL. The voxel sensitivity function in Fourier transform imaging: applications to magnetic resonance angiography. Magn Reson Med 1995;33:156–162.
12. Du YP, Parker DL, Davis WL, Cao G. Reduction of partial-volume artifacts with zero-filled interpolation in three-dimensional MR angiography. J Magn Reson Imaging 1994;4:733–741.
13. Fuderer M. The information content of MR images. IEEE Trans Med Imaging 1988;7:368–380.
14. Kreyzsig E. Advanced engineering mathematics. New York: John Wiley and Sons; 1972. p 314.
15. Hedges LK, Sobering G. Realizing the intrinsic resolution in MRI data. In: Proceedings of the 2nd Meeting of SMR, 1994. p 839.
16. Cooper TG, Siebert JE, Meyer B, et al. Improved magnetic resonance angiography vessel edge definition with truncated sinc interpolation. In: Proceedings of the 4th Annual Meeting of ISMRM, New York, 1996. p 1609.
17. Avinash GB. Band limited interpolation and projection of spatial 3-D images. U.S. patent 5923789.

18. Bernstein MA. Are the corners of k-space worth preserving? In: Proceedings of the 3rd Meeting of SMR, 1995. p 734.
19. Lowe MJ, Sorenson JA. Spatially filtering functional magnetic resonance imaging data. Magn Reson Med 1997;37:723–729.
20. Maudsley AA, Matson GB, Hugg JW, Weiner MW. Reduced phase encoding in spectroscopic imaging. Magn Reson Med 1994;31:645–651.
21. Scheid F. Schaum's outline series: theory and problems of numerical analysis. New York: McGraw Hill; 1968. p 405.
22. Hugg JW, Maudsley AA, Weiner MW, Matson GB. Comparison of k-space sampling schemes for multidimensional MR spectroscopic imaging. Magn Reson Med 1996;36:469–473.
23. Van Gelderen P. Comparing true resolution in square versus circular k-space sampling. In: Proceedings of the 6th Annual Meeting of ISMRM, Sydney, Australia, 1998. p 424.
24. Bernstein MA. Angular dependence of spatial resolution in images interpolated with zero-filling. In: Proceedings of the 7th Annual Meeting of ISMRM, Philadelphia, 1999. p 177.
25. Wilman AH, Riederer SJ. Performance of an elliptical centric view order for signal enhancement and motion artifact suppression in breath-hold three-dimensional gradient echo imaging. Magn Reson Med 1997;38:793–802.
26. Huston III J, Fain SB, Riederer SJ, et al. Carotid arteries: maximizing arterial to venous contrast in fluoroscopically triggered contrast-enhanced MR angiography with elliptic centric view ordering. Radiology 1999;211:265–273.
27. Fain SB, Riederer SJ, Bernstein MA, Huston III J. Theoretical limits of spatial resolution in elliptical-centric contrast-enhanced 3D-MRA. Magn Reson Med 1999;42:1106–1116.